Elaboration of epoxy/silica composites by cationic photopolymerization: Kinetic study, optical and mechanical characterization

Cyrielle Ibanez, Laurence Lecamp, Fabien Boust, Philippe Lebaudy, Fabrice Burel

Version of Record: https://www.sciencedirect.com/science/article/pii/S1010603020305979
Manuscript_257db05158e90474c70f2afe5ed7f33c

Elaboration of epoxy/silica composites by cationic photopolymerization: kinetic study, optical and mechanical characterization

Cyrielle Ibanez, Laurence Lecamp*, Fabien Boust, Philippe Lebaudy, Fabrice Burel

Normandie Université, INSA de Rouen, CNRS UMR 6270, FR 3038, Avenue de l'Université, F-76801 SAINT ETIENNE DU ROUVRAY Cedex, France

Abstract

Thick epoxy composite materials (> 1 mm) have been elaborated by a room temperature process involving photopolymerization through a cationic pathway. Two epoxy resins (glycidyl ether and cycloaliphatic) were chosen as model organic matrix whereas microspherical silica particles (until 50 wt-%) were used as reinforcement. The monitoring of the photopolymerization kinetics by FTIR spectroscopy has first shown the existence of a conversion gradient in the material thickness, which resulted either from light absorption by the matrix and/or from light scattering induced by the presence of filler. More especially, the light scattering was found to be all the more important as the refractive index gap between filler and matrix was high. However, this conversion heterogeneity has then been able to be compensated by ageing involving a postpolymerization reaction at room temperature. The analysis of the mechanical properties of the obtained materials has confirmed that it was possible to obtain thick photocomposite materials homogeneously crosslinked. This homogeneity was even enhanced by using a radiation in the 300-440 nm wavelength range.

Keywords: cationic photopolymerization; epoxy composite; light scattering; refractive index; postpolymerization

* Corresponding author
E-mail: laurence.lecamp@insa-rouen.fr

1. Introduction

The reduction in the consumption of fossil resources is currently a major economic and ecological issue. This is the case in aeronautic and automobile fields where industries seek to reduce the weight of appliances and thus fuel consumption. In this context, for several decades, the replacement of a maximum of metal parts with plastic materials presenting equivalent mechanical, thermal, electrical and chemical resistance properties but with a much lighter weight is privileged. Composites answer to these criteria with a wide choice of materials, reinforcements, matrices and techniques of implementation widely developed and still under development in a process of continuous improvement.

The photochemical process can be an interesting method for composite elaboration. Indeed, it has many advantages, such as easy implementation, extremely fast reaction rates, spatiotemporal control, low energy consumption and no VOC emissions. However, the main disadvantage of this process is the photopolymerizable thickness which is limited to a few hundred micrometers because of light absorption by the polymerizable medium (Beer-Lambert law) [1]. For this reason, the photopolymerization process is widely used in the field of coatings, paints, surface treatments, electronic ... but much less trivial in the field of composite applications. Indeed, an additional phenomenon of light absorption and/or scattering is induced by the presence of fillers, resulting in a decrease of the light intensity required for the photoinitiation step [2-4]. If the absorption is inherent to the chemical nature of the reactants used, the light scattering can be more or less controlled. Thus, two ways are usually put forward to overcome the light scattering phenomenon: (i) reducing the size of the reinforcement below the critical light scattering wavelength, typically below 200 nm ; this involves the use of nanoscale fillers [5], but this solution does not always give the expected properties for the targeted application and exhibits toxicological risks ; (ii) matching the

refractive indices of matrix and fillers ; indeed, the smaller the refractive index gap between filler and matrix, the lower the light scattering, and consequently the higher the light transmittance efficiency [6-9]. Thus, fillers become optically transparent for the radiation, which makes it possible to homogeneously polymerize the matrix and, therefore, to obtain a material having optimal mechanical properties on a greater thickness [10]. However, this second approach is subjected to two important constraints. The first one is that the refractive index of the organic matrix varies versus conversion degree and temperature [11-14]. The second constraint is that a bad filler/matrix interface due to the presence of voids around the filler and resulting from a volume shrinkage during the photopolymerization, a poor wetting of the fillers by the matrix or a different thermal expansion of the matrix in relation to fillers, can generate light scattering/reflection and accentuate this heterogeneity.

In a previous paper [10], conversion profiles inside thick composite sample were predicted by numerical modeling as a function of the matrix composition. This modeling considered the refractive index variation of an acrylic matrix in the course of polymerization and demonstrated the influence of the refractive index gap between matrix and filler on the material homogeneity. This work is part of the continuity of this previous study and aims to experimentally characterize the influence of the refractive index gap between matrix and fillers on the homogeneity of photocomposites in terms of conversion and mechanical properties. Epoxy matrices were chosen since they are commonly used in composite materials and present the advantage of low volume shrinkage (up to 7% [15,16]) compared to (meth)acrylate resins (up to 15% [17]) usually used in photopolymerization. In this way, problems at the filler/matrix interface should be minimized. Micrometric silica particles were selected as reinforcement for their refractive index near to the matrix one.

This paper is divided into two parts. First, photopolymerization kinetics are investigated on thick (un)loaded formulations in order to characterize the influence of light

absorption and/or scattering phenomena on the conversion profiles. The evolution of the medium transparency in the course of its photopolymerization is also studied in relation to the matrix refractive index variation. Then, we interest in determining if the light absorption and/or the refractive index difference between fillers and matrix (potentially inducing a conversion gradient) impact the mechanical properties of the resulting photocomposites.

2. Materials and methods

2.1. Materials

Trimethylolpropane triglycidyl ether (TMPGE, Sigma-Aldrich), (bis(3,4-epoxycyclo-hexylmethyl) adipate (Cyracure™ UVR6128, Dow) and (4-methylphenyl)[4-(2-methylpropyl) phenyl] hexafluorophosphate iodonium (Irgacure 250, BASF) were used as received (Scheme 1). Silica particles with spherical form and a 30-50 µm average diameter were purchased from Biovalley.

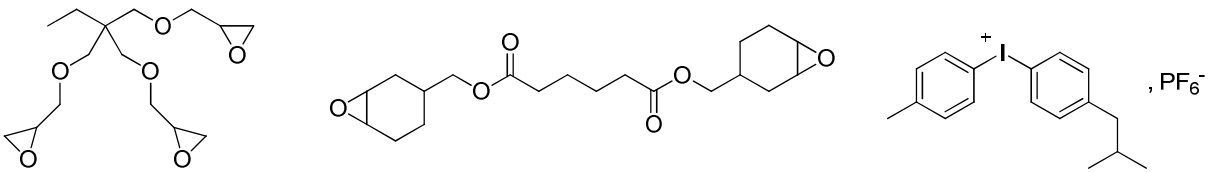

Scheme 1 Chemical formula of reactants

3 wt-% Irgacure 250, used as photoacid generator, were added in each resin and the mixture was stirred at room temperature. As required, silica particles were added in the photopolymerizable formulation at different weight percentages. The composite formulation was homogenized with a Speedmixer™.

2.2. Photopolymerization kinetics monitoring

The polymerization progress was followed at a controlled temperature by real time infrared spectroscopy using a Vertex 70 FTIR spectrometer (Brüker). An attenuated total reflection accessory (ATR MKII Golden Gate, Specac, Eurolabo) was used. The photocurable mixture was deposited out over the ATR diamond crystal in different thicknesses and exposed to a radiation coming from a polychromatic Hg-Xe lamp (Hamamatsu LC8). This technique allows measuring the epoxy conversion on the sample side which is not directly exposed to the UV radiation. By varying the photocured sample thickness, conversion profiles within sample thickness can be achieved. The light intensity was measured at the sample surface using a radiometer (Vilber - Intraspec Oriel VLX-3W) fitted with a probe at 254 or 365 nm. When required, a cutoff filter (Hamamatsu A9616-05) was added to limit the irradiance spectrum to wavelengths ranging from 300 to 440 nm.

The absorbance of each functional group was determined by the area (A) of the corresponding absorption peak. Thus, for UVR6128, the conversion χ was calculated using the ratios of the epoxy absorbance (A^{epoxy}) at 788 cm^{-1} to a reference absorbance (A^{ref}) corresponding to the carbonyl group at 1726 cm^{-1} as follows:

$$\chi(t) = \frac{\frac{A_0^{epoxy}}{A_0^{ref}} - \frac{A_t^{epoxy}}{A_t^{ref}}}{\frac{A_0^{epoxy}}{A_0^{ref}}} \times 100$$

where A_0 is the initial area and A_t is the area of the peak at t time.

For TMPGE, no reference could be used. Therefore, the conversion χ was calculated as follows:

$$\chi(t) = \frac{A_0^{epoxy} - A_t^{epoxy}}{A_0^{epoxy}} \times 100$$

2.3. Refractive index measurement

The refractive index was measured at 30°C and 659 nm using an Arago refractometer (Cordouan Technologies). For solid materials, the refractive index was determined by immersion in solvent mixture whose composition was varied until visual disappearance of the solid in the liquid phase. The refractive index of the solvent mixture which is the same as the solid one was measured using the Arago refractometer.

2.4. Absorbance measurement

The UV-visible spectra were carried out on a Varian Cary 50 UV-visible spectrometer. Solutions in acetonitrile were analyzed from 200 to 600 nm.

2.5. Light transmittance measurement

Light transmittance measurement was carried out using an integrating sphere and a Maya2000-Pro spectrophotometer from Ocean Optics (I.D.I.L. Fibres Optiques) [18]. The light intensity coming from a polychromatic Hg-Xe lamp (Hamamatsu LC8) was limited to the range 300-440 nm by using a cutoff filter (Hamamatsu A9616-05). The relative light transmittance was calculated as follows:

$$T = \frac{I_t}{I_0}$$

where I_t and I_0 are the intensities transmitted and received by the sample at 403 nm, respectively.

2.6. Epoxy conversion measurement on thick photocured samples

1 mm thick photocured samples were analyzed by differential scanning calorimetry (DSC Q2000, TA Instruments). Samples were submitted to a 10°C/min heating rate, from -25

to 330°C, under nitrogen atmosphere (50 mL.min^{-1}). Conversion of epoxy groups was determined as follows:

$$\chi(t) = \frac{\Delta H_{theor} - \Delta H_{res}}{\Delta H_{theor}} \times 100$$

where ΔH_{res} is the residual reaction enthalpy measured by DSC and ΔH_{theor} is the theoretical enthalpy corresponding to a 100% conversion in epoxy functions (ΔH_{theor} = -75 to -100 kJ/mol[19] for oxirane group, i.e. ΔH_{theor} = - 744 to - 992 J/g for TMPGE, and ΔH_{theor} = - 95.3 kJ/mol[19] for cycloaliphatic epoxy group, i.e. ΔH_{theor} = - 520.1 J/g for UVR6128).

2.7. Mechanical properties measurement

Photocured samples (10 x 40 x 1 mm) were analyzed by dynamical mechanical analysis (DMA Q800, TA Instruments) in single cantilever mode at a 1 Hz frequency and a 3°C/min heating rate. The applied strain amplitude was 60 µm. The mechanical transition temperature T_α was measured at the maximum of the tan δ curve.

An adaptation of Einstein's formula developed by Guth [20] allowed calculating the theoretical composite storage modulus E'_c as a function of the filler volume fraction (V_f) according to the following formula:

$$E'_c = E'_m\left(1 + 2{,}5V_f + 14V_f^2\right)$$

where E'_m is the storage modulus of the unloaded matrix.

The theoretical maximum height of tan δ, i.e. tan δ_c, can also be calculated according to the Nielsen equation [21,22]:

$$\tan\delta_c = \tan\delta_m(1 - V_f)$$

where tan δ_m is the maximum height of tan δ of the matrix.

3. Results and discussion

To carry out this study, two epoxy monomers were chosen as model molecules: the trimethylolpropane triglycidyl ether (TMPGE) belonging to the epoxy glycidyl ether family, and the bis(3,4-epoxycyclo-hexylmethyl) adipate (UVR6128) depicting the family of epoxy cycloaliphatic monomers.

3.1. Influence of the matrix absorption on conversion profiles of thick unloaded formulations

In order to characterize the influence of the matrix absorption on the polymerization progress, photopolymerization kinetics were first followed by real time IR spectroscopy on unloaded samples with different thicknesses. Fig. 1 presents the epoxy conversion curves versus irradiation time at 40°C and an incident light intensity of 63 mW/cm² measured at 254 nm.

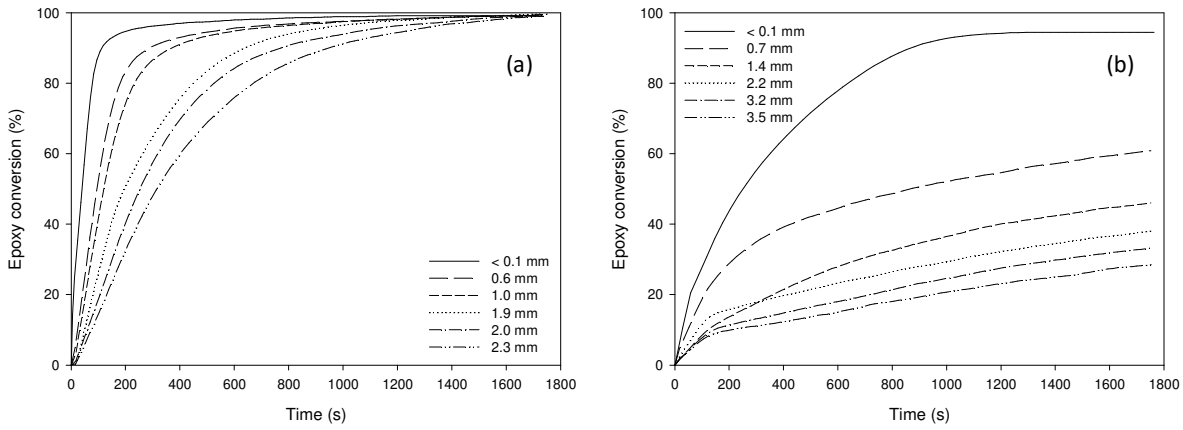

Fig.1 Conversion kinetics of (a) TMPGE and (b) UVR6128 versus sample thickness – T = 40°C – I_0 = 63 mW/cm² at 254 nm

Fig. 1a shows that, in the case of TMPGE, the conversion of epoxy groups is not limited by the sample thickness (over the studied range) since a 100% conversion is reached after 30 minutes of irradiation. Only kinetics is impacted: the greater the thickness, the slower the polymerization. In contrast, for UVR6128 (Fig. 1b), kinetics and final conversion decrease

when the sample thickness increase. The different behavior of both resins is due to two various phenomena. First, TMPGE is more reactive than UVR6128. Thus, 100% conversion are reached faster for TMPGE than for UVR6128. Secondly, TMPGE exhibits a lower absorbance in the efficiency wavelength range of the photoinitiator than UVR6128 (see Fig. SI.1), favoring a better light penetration within the sample thickness. Therefore, the ultimate epoxy conversion is impacted by the matrix absorbance only in the case of UVR6128.

3.2. Influence of light scattering on conversion profiles of thick loaded formulations

Biovalley silica was selected as filler for its refractive index value (n = 1.5123 at 659 nm) close to that of the studied epoxy matrices. As shown in Table 1, before photopolymerization, initial refractive index (n_i) of both resins is lower than the silica one. After UV irradiation, the refractive index of the matrix was increased as expected. Thus, whatever the epoxy resin considered, the final refractive index (n_f) of the polymerized matrix has come closer to the silica one, although always below. The refractive index differences between filler and matrix before photopolymerization (Δn_i) and after photopolymerization (Δn_f) are also reported in Table 1. Δn_i is weaker for the UVR6128 resin-based loaded formulation. This formulation is therefore initially less light scattering than the one based on TMPGE. At the end of polymerization, Δn_f is also lower for UVR6128, suggesting a final material more transparent towards light compared to TMPGE.

Table 1 Refractive index values at 659 nm and 30°C of (un)loaded and/or photopolymerized epoxy resins

Resin	Before photopolymerization		After photopolymerization		$\Delta n = \Delta n_i - \Delta n_f$
	n_i	Δn_i	n_f	Δn_f	
TMPGE	1.4738	0.0385	1.4942	0.0181	0.0204
UVR6128	1.4830	0.0293	1.4999	0.0124	0.0169

n_i: refractive index of the monomer; n_f: refractive index of the polymer; Δn_i: refractive index difference between filler and monomer; Δn_f: refractive index difference between filler and polymer; Δn: refractive index gain consecutive to polymerization

We therefore have two composite formulations with different optical properties: one, based on the epoxy glycidyl ether TMPGE, is characterized by a low absorbance in the UV range but an important light scattering (high Δn), the other, based on the cycloaliphatic epoxy UVR6128, exhibits a higher UV absorbance but a weaker light scattering (low Δn). These two formulations are going to be studied in order to characterize the impact of Δn on the photopolymerization and, subsequently, on the mechanical properties of the photocomposites.

A kinetic study similar to the previous one was first carried out on thick loaded formulations (1.8 mm thick for TMPGE, 1.4 mm thick for UVR6128) in order to characterize the influence of fillers on conversion profiles. Fig. 2 presents the epoxy conversion curves versus irradiation time for both resins submitted to the same irradiation conditions. As far as the photopolymerization of the UVR6128 resin is concerned, Figure 2b shows that the kinetic curves are weakly impacted by the addition of silica particles. Indeed, one can observe a perfect superposition of the curves at the beginning of the reaction and then a slight gap with each other. The final conversion difference between resin alone and 30 wt-% loaded formulation is only 5% after 30 min of irradiation. In contrast, the photopolymerization of the TMPGE resin (Fig. 2a) is more impacted. Indeed, the higher the silica weight percentage, the lower the kinetics and the final conversion. A decrease of 20% in the final conversion is

observed when adding 30 wt-% fillers compared to the unloaded formulation. This difference can be correlated to the Δn (initial and final) values. Thus, in the case of UVR6128 for which light scattering is less, a more uniform polymerization is obtained within the sample thickness. For the more light-scattering TMPGE-based formulation, the photopolymerization is more heterogeneous within thickness.

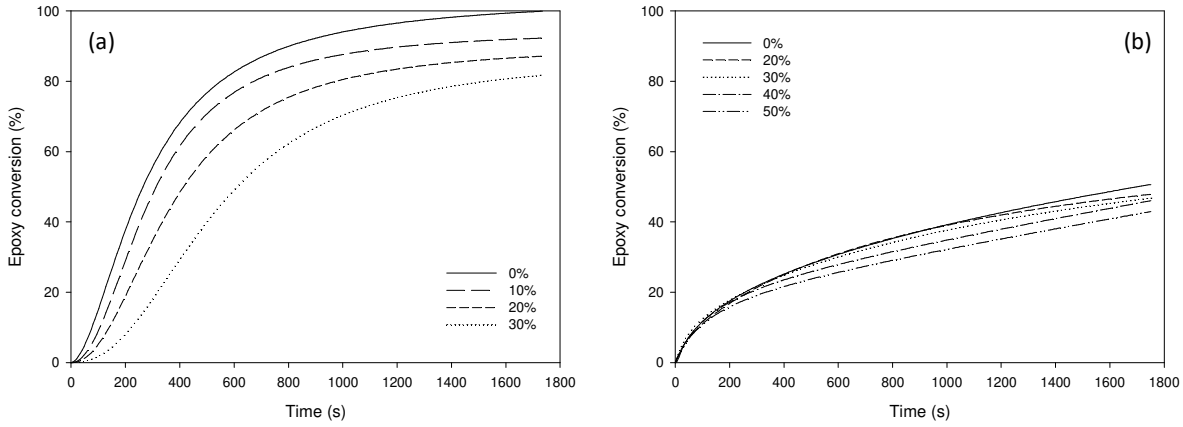

Fig. 2 Conversion kinetics of (a) TMPGE (1.8 mm thick) and (b) UVR6128 (1.4 mm thick) versus silica rate – T = 40°C – I_0 = 63 mW/cm² at 254 nm

In parallel, the evolution of the medium transparency during photopolymerization was followed by means of a device comprising an integrating sphere fitted with a spectrophotometer (Scheme 2). Each photocurable formulation was deposited in 1 mm thick layer on a glass slide brought on the top of the integrating sphere. Irradiation of the formulation was then performed in the same conditions of temperature and incident light intensity as on the IR cell. As the radiation crossing the sample and the glass slide is reflected on the entire inner surface of the integrating sphere, the spectrophotometer positioned at the exit of the sphere allows measuring the intensity of the radiation transmitted and scattered by the sample during its photopolymerization. Thus, the more transparent the sample becomes, the higher the collected intensity by the spectrophotometer and the transmittance. Let us note

that, in order to avoid yellowing of the medium that hinders the measurement, the sample was exposed to a radiation limited to wavelengths ranging from 300 to 440 nm.

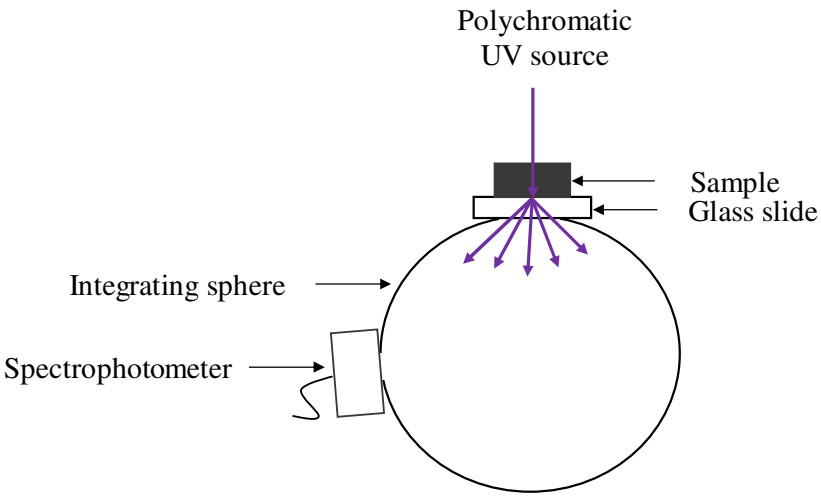

Scheme 2 Experimental device for light transmittance measurement

Fig. 3 shows the evolution of the relative transmittance of each epoxy formulation in the course of photopolymerization. The corresponding conversion curves are also presented.

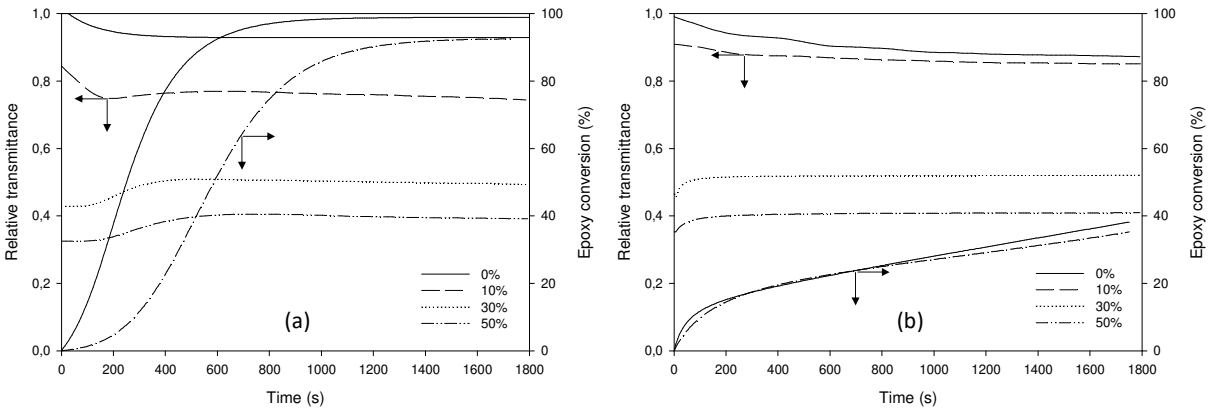

Figure 3 Evolution of relative transmittance at 403 nm and epoxy conversion of (a) TMPGE and (b) UVR6128 versus irradiation time and silica rate – T = 40°C – I_0 = 115 mW/cm² at 365 nm

For both resins and in a logical way, the higher the filler rate, the lower the initial relative transmittance. In the absence of fillers, a slight but continuous decrease in transmittance is observed in the course of photopolymerization. This phenomenon cannot be attributed to an evolution of the sample transparency since this one is optically transparent (no filler). This could rather be related to the volume shrinkage induced by the sample polymerization. Indeed, this phenomenon may result in an alteration of the sample surface state which is less uniform (as shown in Fig. SI.2) and therefore more prone to reflect the incident radiation. One can notice that this phenomenon is slightly more pronounced for TMPGE which is subject to a greater volume shrinkage.

The shape of the relative transmittance curves is significantly different for loaded formulations. In the case of UVR6128 (Fig. 3b), the transmittance in the presence of 10 wt-% of silica varies less but in a similar way compared to UVR6128 alone. On the other hand, for higher silica rates (30 wt-% and 50 wt-%), the transmittance increases at the beginning of the reaction and then stabilizes at a plateau. In a previous study, we showed that the increase in the refractive index of an epoxy resin being photopolymerized is mainly related to the increase in the density of the reaction mixture [14]. Thus, at the beginning of irradiation, the conversion increase leads to an increase of the matrix density and, consequently, of its refractive index. The decrease in Δn between fillers and matrix then results in a transmittance increase. Moreover, it is interesting to note that the stabilization of the radiation transmittance corresponds to the inflection point of the conversion curve, i.e. to the decrease of the reaction rate. This slowdown may be explained by the gelation of the reaction mixture. Indeed, during this step, the conversion of the epoxy groups continues but the matrix density variation is much less. At last, it is noteworthy that the presence of fillers likely attenuates this density variation, so that a stabilization of the medium refractive index and, consequently, of the light transmittance is observed whereas the reaction continues.

In the case of TMPGE (Fig. 3a), a significant drop (about 20%) of the initial transmittance followed by a slight increase to a plateau is observed for the formulation containing 10 wt-% of silica. The passage through a minimum could be explained by a competition between the effect of the volume shrinkage and the decrease of Δn, which would win over the volume shrinkage at high conversions. For higher filler rates, the initial drop in transmittance seems to be masked in favor of a continuous increase to a plateau. The stability of the transmittance during the first 100 seconds of irradiation can be correlated to the low conversion variation and therefore to the low variation of density and refractive index. After this period, the same phenomena than those mentioned previously for UVR6128 can explain the variations observed.

3.3. Mechanical characterization of photocomposites

1 mm thick photocomposites were obtained at room temperature after 2 hours irradiation under an incident light intensity of 30 mW/cm² at 254 nm. The epoxy conversion of these samples was first measured by DSC analyzes performed just after irradiation and after 24 hours ageing at room temperature (Table 2). For that, photocured samples were submitted to a temperature ramp and the measured residual polymerization enthalpy was referred to the theoretical value, as described in the experimental part.

Table 2 Epoxy conversion of photocomposites versus ageing time

Time after irradiation (h)	**Epoxy conversion (%)**	
	TMPGE	**UVR6128**
0	95	75
24	99	97

In the absence of silica, TMPGE sample was almost completely converted (95%) at the end of irradiation while the conversion was only 75% for UVR6128. After 24 hours of ageing, a quasi-complete conversion was reached for both resins, indicating a relatively fast postpolymerization at room temperature. In the end, the postpolymerization erased the conversion gradient (especially for UVR6128), so that materials can be considered as completely crosslinked after ageing. The same observations were carried out on all the prepared photocomposites (average final conversion between 97 and 99% after 24 hours ageing at room temperature).

3.3.1. Study of samples photocured under polychromatic irradiation (no cutoff filter)

Because high volume shrinkage during photopolymerization, the elaboration of composite materials from TMPGE with sufficient controlled geometry for DMA analysis failed under polychromatic irradiation (without cutoff filter). The study under these irradiation conditions was therefore conducted only on UVR6128 resin. DMA analysis was performed on photocured materials stored 24 hours at room temperature. Fig. 4 presents the evolution of storage modulus E' and tan δ versus temperature for (un)loaded photocured materials. As expected, the storage modulus E' was increased in the presence of silica, the reinforcement increasing the rigidity of the material by reducing the mobility of the polymer chains.

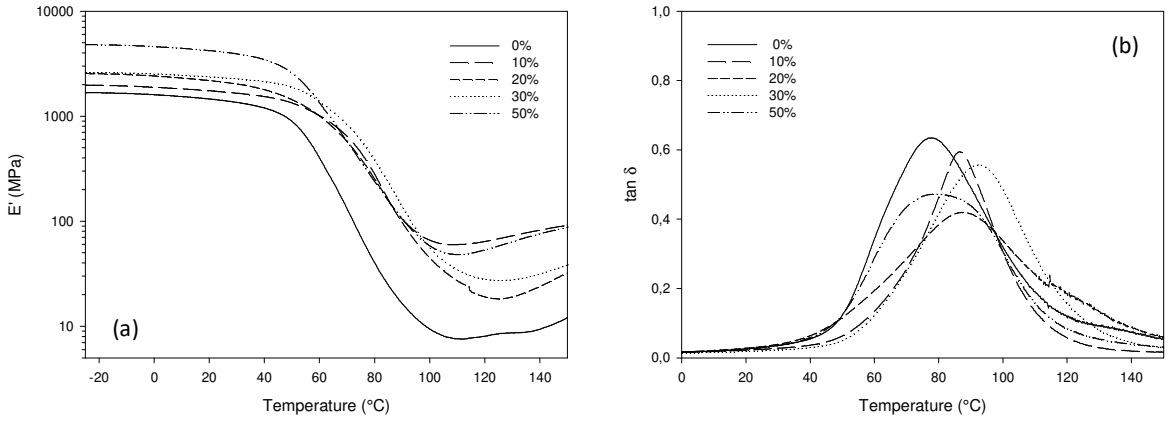

Fig. 4 Evolution of (a) storage modulus E' and (b) tan δ versus temperature and silica rate for 1 mm thick UVR6128 materials photocured under polychromatic radiation

Theoretical and experimental E' values at 25°C (Table 3) are very close, indicating a homogeneous polymerization. This is also consistent with the tan δ curves which exhibit a Gaussian shape. Moreover, whatever the filler rate, the maximum of tan δ is logically lower for composites than for the unloaded matrix because of reduced molecular mobility. Otherwise, the experimental values of tan δ are generally close to the theoretical ones, indicating that the filler-matrix interface would not be optimal. Indeed, experimental values weaker than the theoretical ones suggest a great interfacial interaction between the filler and the matrix and an immobile layer between these two entities [21].

Table 3 Comparison of experimental and theoretical values of E' and maximum of tan δ versus filler rate

Silica (%)	**E' (MPa) at 25°C**		**Maximum of tan δ**		**Tα (°C)**
	Experimental	**Theoretical**	**Experimental**	**Theoretical**	
0	1412	-	0.63	-	78
10	1703	1630	0.59	0.60	86
20	2113	1986	0.42	0.57	88
30	2326	2528	0.56	0.53	92
40	n.d.	n.d.	0.42	0.48	n.d.
50	4082	4484	0.47	0.43	79

n.d.: not determined

Finally, one can also notice a drastic decrease in the material's Tα for silica rates higher than 30 wt-%. This decrease may likely be explained by more important silica-silica interactions than silica-matrix interactions. Below this critical silica rate, Tα logically increases with the filler rate.

3.3.2. Study of samples photocured under limited polychromatic irradiation (with cutoff filter)

Under filtrated radiation, TMPGE-based samples with good control of their geometry were achieved. The elimination of the infrared radiations from the lamp probably allowed limiting the heat favorable to the sample volume shrinkage during photopolymerization. The mechanical properties of composites elaborated under these conditions were therefore characterized for both epoxy resins (Table 4 and Fig. 5). The E' versus temperature curves are available on Fig. SI.3.

Table 4 Comparison of experimental values of E', maximum of tan δ and Tα versus filler rate for thick samples photocured under 300-440 nm radiation

Silica	**E' (MPa) at 25°C**		**Tα (°C)**	
(%)	**TMPGE**	**UVR6128**	**TMPGE**	**UVR6128**
0	1965	1990	78	70
10	2688	2624	78	75
20	3203	3005	77	79
30	3087	3130	79	79
40	2769	3027	78	82
50	2928	3591	78	78

All the materials exhibit a Tα close to 78°C. Table 4 shows that the storage moduli of both (un)loaded resins are very close. Again, for UVR6128, the higher the rate of silica, the higher E' is, indicating the effectiveness of the reinforcement on the rigidity of the material. In contrast, in the case of TMPGE, E' increases with the silica rate until a plateau from 30 wt-% of filler. It therefore seems that an optimal filler rate exists to reinforce a TMPGE matrix. Besides, the maximum of tan δ is much lower for TMPGE than for UVR6128 (Figure 5), indicating a much greater mobility in UVR6128 matrix photocomposites. This may be explained by the higher functionality of the TMPGE (trifunctional) which leads to a more highly crosslinked network than UVR6128 (bifunctional).

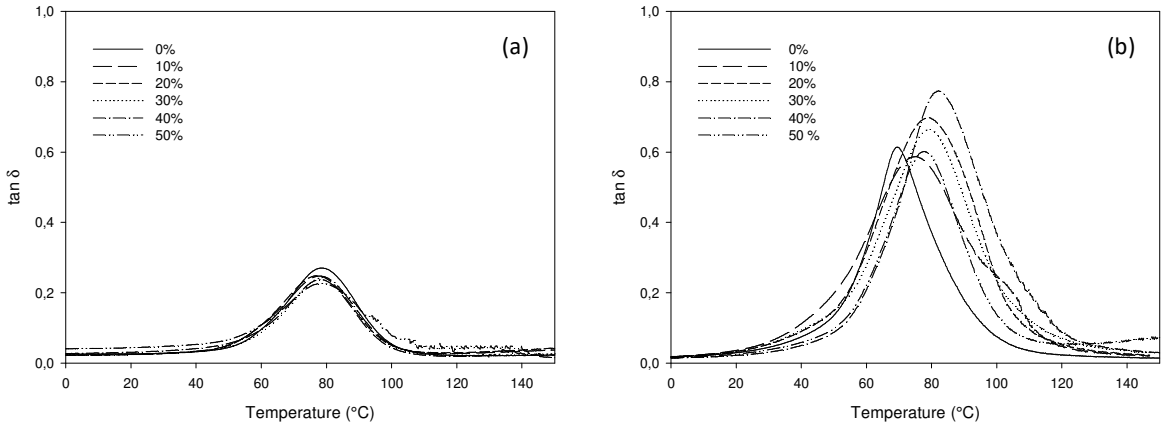

Fig. 5 Evolution of tan δ versus temperature and silica rate for (a) 1 mm thick TMPGE materials and (b) 1 mm thick UVR6128 materials photocured under 300-440 nm radiation

Moreover, it appears that E' values as well as tan δ curves are different according to the irradiation conditions. In a surprisingly way, the weakest moduli correspond to the UVR6128 samples produced without cutoff filter, i.e. when the photopolymerization reaction is faster (Fig. SI.4). A quick reaction seems therefore cause a loss of rigidity, perhaps due to a difference in density of the final material according to the irradiation conditions. Finally, the comparison of tan δ curves (Fig. 4b and 5b) shows that photopolymerization of UVR6128 in

presence of the filter leads to much more homogeneous materials. Indeed, in these conditions, Tα values are less dispersed and height, width and shape of the tan δ curves are closer.

4. Conclusion

The presented study showed that light absorption and scattering may *a priori* be limiting factors for the achievement of homogeneous thick composite materials by photopolymerization. Indeed, these phenomena induce a conversion gradient within the material thickness. Nonetheless, we have shown that, in the case of photocomposites with epoxy matrices, the photoinduced conversion gradient was highly attenuated thanks to the postpolymerization reaction. The homogeneity of these composite materials was further enhanced when the UV curing is carried out under radiation limited to the range 300-440 nm. In the range of thicknesses investigated in this work, it therefore seems quite possible to elaborate homogeneous thick epoxy/silica composites under UV curing.

A way forward to enhance the efficiency of photocomposite production without any energy source other than UV radiation would be to be able to would be to be able to fine-tune the chemical composition of both matrix and fillers, so that their refractive indices can equalize over the entire wavelength range of radiation. This could allow minimizing the initial photopolymerization gradient in a more pronounced way, which would be specially interesting for system with no postpolymerization.

Acknowledgments

The authors thank the Région Normandie for financial support (E2M2 - Poly 3D).

This manuscript is a tribute to the 50-year anniversary of the French Polymer Group (Groupe Français des Polymères - GFP).

References

[1] Garra P, Dietlin C, Morlet-Savary F, Dumur F, Gigmes D, Fouassier JP, Lalevée J, Photopolymerization of thick films and in shadow areas: A review for the access to composites. Polym Chem 2017;8:7088-101.

[2] Bayou S, Mouzali M, Aloui F, Lecamp L, Lebaudy P, Simulation of conversion profiles inside a thick dental material photopolymerized in the presence of nanofillers. Polymer 2013;45:863-70.

[3] Chartier T, Badev A, Abouliatim Y, Lebaudy P, Lecamp L, Stereolithography process: Influence of rheology of silica suspensions and of medium on photopolymerization kinetics-cured depth and width. J Eur Ceram Soc 2012;32:1625-34.

[4] Liu F, Jiang X, Zhang Q, Zhu M, Strong and bioactive dental resin composite containing poly(Bis-GMA) grafted hydroxyapatite whiskers and silica nanoparticles. Compos Sci Technol 2014;101:86-93.

[5] Kudo S, Nagase K, Kubo S, Sugihara O, Nakagawa M, Optically transparent and refractive index-tunable ZrO_2/photopolymer composites designed for ultraviolet nanoimprinting. Jpn J Appl Phys 2011;50:06GK12/1-06GK12/7.

[6] Suzuki H, Taira M, Wakasa K, Yamaki M, Refractive-index-adjustable fillers for visible-light-cured dental resin composites: preparation of TiO_2-SiO_2 glass powder by the sol-gel process. J Dent Res 1991;70:883-88.

[7] Shortall AC, Palin WM, Burtscher P, Refractive index mismatch and monomer reactivity influence composite curing depth. J Dent Res 2008;87: 84-8.

[8] Krug III DJ, Asuncion MZ, Popova V, Laine RM, Transparent fiber glass reinforced composites. Compos Sci Technol 2013;77:95-100.

[9] Fujita K, Nishiyama N, Nemoto K, Okada T, Ikemi Y, Effect of base monomer's refractive index on curing depth and polymerization conversion of photo-cured resin composites. Dent Mater J, 2005;24:403-8.

[10] Aloui F, Lecamp L, Lebaudy P, Burel F, A numerical tool for studying photopolymerization inside thick composites: Influence of optical properties on the conversion profiles for a silica/TEGDMA-BisGMA formulation. J Photochem Photobiol A Chem 2018;356:418-24.

[11] Hadis MA, Tomlins PH, Shortall AC, Palin WM, Dynamic monitoring of refractive index change through photoactive resins. Dent Mater 2010;26:1106-12.

[12] Howard B, Wilson DN, Newman SM, Pfeifer CS, Stansbury JW, Relationships between conversion, temperature and optical properties during composite photopolymerization. Acta Biomaterialia 2010;6:2053-59.

[13] de Boer J, Visser RJ, Melis GP, Time-resolved determination of volume shrinkage and refractive index change of thin polymer films during photopolymerization. Polymer 1992;33:1123-26.

[14] Aloui F, Lecamp L, Lebaudy P, Burel F, Photopolymerization of an Epoxy Resin: Conversion and Temperature Dependence of its Refractive Index. Macromol Chem Phys 2016;217:2063-67.

[15] Zarrelli M, Skordos AA, Partridge IK, Plastics, Rubber and Composites Processing and Applications 2002;31:377-384.

[16] Vijayan PP, Pionteck J, Huczko A, Puglia D, Kenny JM, Thomas S, Liquid rubber and silicon carbide nanofiber modified epoxy nanocomposites: Volume shrinkage, cure kinetics and properties. Compos Sci Technol 2014;102:65-73.

[17] Koseki K, Sakamaki H, Jeong KM, In situ measurement of shrinkage behavior of photopolymers. J Photopolym Sci Technol 2013;26:567-572.

[18] Azan V, Lecamp L, Lebaudy P, Bunel C, Simulation of the photopolymerization gradient inside a pigmented coating. Influence of TiO_2 concentration on the gradient. Prog Org Coat 2007;58:70-5.

[19] Brandrup J, Immergut E, Polymer Handbook (Wiley & Sons, 1975).

[20] Guth E, Theory of filler reinforcement. J Appl Phys 1945;16:20-5.

[21] Idicula M, Malhotra SK, Joseph K, Thomas S, Dynamic mechanical analysis of randomly oriented intimately mixed short banana/sisal hybrid fibre reinforced polyester composites. Compos Sci Technol 2005;65:1077-87.

[22] Vasudevan A, Kumaran S, Naresh K, Velmurugan R, Experimental and analytical investigation of thermo-mechanical responses of pure epoxy and carbon/Kevlar/S-glass/E-glass/epoxy interply hybrid laminated composites for aerospace applications. Int J Polym Anal Charact 2018;23:591-605.

Relation between Activator Ratio, Hydration Products and Mechanical Properties of Alkali-activated Slag

Ugo De Filippis[a], Elodie Prud'homme[a,*], Sylvain Meille[a]

[a] *Univ Lyon, INSA Lyon, MATEIS UMR 5510, 7 avenue Jean Capelle, 69100 Villeurbanne, France*

**Corresponding author: elodie.prudhomme@insa-lyon.fr*

The use of cement substitute, such as alkali-activated slag, is of great interest in the field of earth-based construction materials to preserve their environmental benefit. Nonetheless, the cationic activity of clayey particles of earth-based materials induces new issues by affecting the alkaline conditions in which slag is activated. This work aims to present how alkaline conditions modify the nature and the amount of hydrates formed, the kinetics for reaction and the resulting mechanical properties. A minimum of 5 wt.% of activator with respect to the slag was needed to trigger consolidation of the samples within the first 24 hours, while an activator content of 15% led to an excess of sodium, especially remarkable at early age. Besides, hydration kinetics were followed *in situ* during the first 3 days by infrared spectroscopy. The formation of portlandite and hydrotalcite-like hydrates were only observable from 10% of activator and the presence of hydrotalcite is correlated with an increase in mechanical properties. Finally, these results are of interest for the formulation of earth-based materials by predicting hydrated phases formed during slag activation depending on alkaline conditions.

Keywords: Compressive strength, In-situ FTIR, Thermal analysis, Hydrates assemblage, SEM-EDX

1. Introduction

Grounded Blast Furnace Slag (GBFS) is a steel industry by-product commonly used as Ordinary Portland Cement (OPC) substitute because of its lower environmental footprint. Reducing OPC consumption, whose production is responsible for 5 to 7% of worldwide carbon dioxide emissions [1,2], is a critical issue and the use of alternative cementitious binder is an attractive option. Blast furnace slag presents a latent hydraulicity, meaning that under specific activation conditions it can dissolve and lead to the formation and growth of hydrates similar to those observed during OPC hydration [3]. This opens the way for applications as building materials, soil stabilization, and reinforcement of earth-based concrete or bricks [4,5].

Soil stabilization with binder adjunction, as OPC or activated slag, consists in the addition of a hydraulic binder to a soil to obtain a hydrated composite material. Interactions between binder's hydrates and soil's particles are of two kinds: physicochemical interactions between hydrated gel and clays particles surface, and pozzolanic reactions between calcium hydroxide potentially released during hydration and clay minerals [4,6]. To better understand these interactions a detailed knowledge of the binder hydration, of the microstructure formed and of the composition of hydrated phases are needed.

Slag hydration has been largely studied in literature [3,7–25,28,30–32,35–39]. As for OPC, it starts with the dissolution of the anhydrous grains into dissolved silicate, aluminate and cationic (sodic or calcic) species. Once these species reach a sufficient concentration in the interstitial solution, they start to precipitate into hydrated phases. This precipitation, lowering the concentration of dissolved species, favors further dissolution of anhydrous grains. However, unlike OPC, slag dissolves very slowly into pure water [7], so that its hydration kinetic is very slow [8], compromising its use as hydraulic binder. To accelerate the initial dissolution an alkaline activator is needed. This activation can be calcic, sodic or sulfatic and usually involves a pH value above 12.5 [9,26]. The cationic species of the activator act as network modifiers and induce a faster dissolution of silicate and aluminate species that compose the glassy structure of anhydrous slag [27]. Cationic species could also prevent the precipitation of calcium aluminate hydrate gel on the grain surface that could hinder further dissolution or ionic diffusion [27]. Previous studies showed that slag's hydration largely depends on its chemical composition, on its particle size distribution, and on the nature of the activation mix [3,9,28–30,10–16,26]. A detailed study of the activation of one particular slag

should then be made in order to characterize the hydrated products formed depending on activation conditions. Currently, the most commonly used mixtures for slag activation are composed of sodium hydroxide and/or sodium silicate, mainly because they lead to the highest properties after activation, such as compressive strength [31,32]. Sodium silicate usually leads to the highest mechanical properties [17], but its production process negatively impacts the environmental footprint of alkali-activated binders [18,33,34]. The influence of the activator concentration in the initial mix has also been investigated. It seems that no consensus has been reached since some authors describe the optimum range of sodium hydroxide content between 3 to 5% of slag mass [19,20,35] while others have shown an increase of hydrated slag's mechanical performance with sodium hydroxide concentration until more than 6 to 10% of slag mass [36,37]. Besides, identification of hydrated phases has been mainly studied in a small range of activator ratio, typically between 2 and 6 wt.%. Sodium hydroxide activation mainly favors the precipitation of hydrated phases such as calcium silicate hydrates and calcium-aluminum silicate hydrates - C-S-H and C-A-S-H respectively - [21,26,29,38], calcium aluminum hydrate gel (CAH) [22,39] and hydrotalcite ($Mg_wAl_xCO_3(OH)_y \cdot z(H_2O)$) [13,23] with GBFS containing high amount of MgO (> 5% wt.) [11,24]. In the objective of soil stabilization, cationic activity of clayed materials allow cationic exchange between clay sheets and interstitial pore solution [40]. This changes the activator concentration and alkaline conditions in which slag is activated. A precise knowledge of the impact of alkaline conditions on slag hydration is therefore needed to understand how cationic activity of clays could disturb slag activation.

The aim of this study is to characterize slag hydration under different alkaline conditions, at early age and in the long term, to understand the impact of initial activator content on the formation and evolution of hydrated phases formed. To take into account these activator's variations, sodium hydroxide is used as activator, considering a large range of Na_2O to slag mass ratios, from 1.25 to 15% of slag mass. These activation rates were chosen because of the end application for earth building materials, which will result in cation exchange with clays. The microstructural characterization, as a function of curing time until 90 days, will then be related to compressive strength measurements.

2. Material and Methods

2.1. Materials

The slag used in this study is a GBFS supplied by ECOCEM France whose composition is given in Table 1. Its specific surface area (Blaine) is 4450 cm²/g and its median diameter (d_{50}) is 11 µm. Basicity of this slag, characterized by (CaO + MgO)/SiO_2 molar ratio, is of 1.19, an indicator of its good reactivity since this ratio is larger than 1 [25].

Table 1: Chemical composition (oxides weigth%) of the slag

Elements	**CaO**	**SiO_2**	**Al_2O_3**	**MgO**	**SO_3**	**Others**
Rate (%)	42.0	35.3	10.9	7.5	2.3	2.0

Activating solutions were prepared by dissolving different amounts of sodium hydroxide pellets (purity 99.9%, Fisher Scientific) in distilled water, as shown in Table 2. Solutions were used after that complete dissolution and cooling to room temperature (25 ± 2°C) was achieved.

2.2. Specimen preparation

Samples were prepared mixing anhydrous slag and activating solutions with a constant water to slag ratio (W/S) equal to 0.4 for each formulation. Pastes were formulated to achieve four different Na_2O to slag weight ratios (A/S): 1.25, 5, 10, and 15%, corresponding to 1, 4, 8, and 12 M NaOH activating solution respectively (Table 2). After a constant hand mixing time (1 min), fresh pastes are poured into cylindrical molds of 2 cm diameter and 4 cm height. Molds are kept closed to stay under endogenous conditions and avoid water evaporation or drying gradient. Samples are demolded after 24 hours, immediately and individually sealed in tightly closed plastic film to stay under endogenous conditions before testing and kept at room temperature. Three samples of each formulation were prepared and tested at 24 hours, 7, 28 and 90 days respectively. All characterization methods were performed at the mentioned curing times and averaged on three samples.

Table 2: Activating solution characteristics used for each initial activator ratio

Activator	Na_2O			
Activator / Slag (wt.%)	1.25	5	10	15
Water / Slag (wt.%)	0.4	0.4	0.4	0.4
$[Na^{2+}]$ (M)	1.01	4.03	8.06	12.1
pH value	13.2	13.6	13.8	13.9

2.3. Characterization Methods

Mechanical properties were determined by uniaxial compressive tests using a Zwick device equipped with a 100 kN load cell (class 0.5). The crosshead speed was set to 0.3 mm/min.

Fourier Transform Infrared spectroscopy (FTIR) were performed on a TermoFisher Scientific IS50 device using Attenuated Total Reflection (ATR) mode from 4000 to 450 cm^{-1}, with a spectral resolution of 0.5 cm^{-1} and averaged on 32 scans. Data were acquired with Omnic Series software with the same parameters for both the tests on hydrated samples and for the *in situ* experiments. Data were analyzed using Omnic Series software with a baseline correction treatment. All spectra were normalized with respect to the water absorbance band at 1640 cm^{-1}.

For the characterization of hydrated paste at each curing time, sample pieces were used without prior grinding. *In situ* infrared experiments were conducted using a plastic mold fixed on ATR tool's plate and centered on the crystal (Figure 1). It allows pouring slag paste onto analysis area just after mixing (1' mixing + 45'' pouring). A piston inserted into the mold maintained a constant pressure on the sample and ensured a good contact with ATR crystal. Water evaporation was limited using a water tank around the mold and the whole system was covered with a plastic film. Scans were obtained using the same parameters as described hereinabove with a time step of 1 minute during 3 days. The first (after 1min) and the last (after 3 days) spectra obtained with this technique are available for all formulations in the supplementary material.

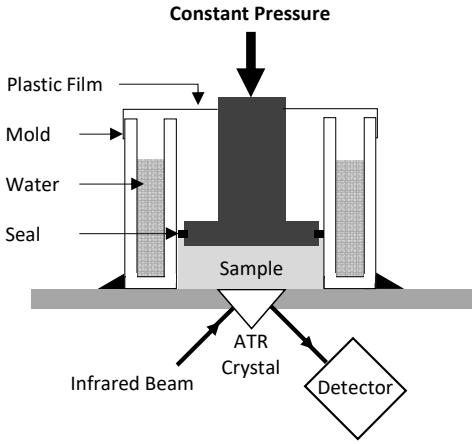

142

143 *Figure 1: Scheme of infrared (ATR) setup for in situ follow-up of hydration*

144

145 Thermogravimetric (TGA) and differential thermal analysis (DTA) were performed on a
146 Setaram Setsys Evolution device (Caluire, France) up to 1050°C with a heating rate of
147 10°C/min and under dry air with a fixed flow of 20 mL/min. A 50.0 ± 0.5 mg mass is placed
148 in a closed alumina crucible. Measurements data are analyzed with Setsoft software. Baseline
149 corrections are operated with a blank measurement realized on an empty alumina crucible.

150

151 X-ray diffraction patterns were acquired with a D8 Advance diffractometer (Brucker,
152 Germany) using CuKα radiation (λKα = 0.154186 nm), an acquisition step of 0.02° (2θ)
153 between 5° and 65° (2θ), and a dwell time of 1.3 s. The analysis is carried out on a plane
154 surface of the sample that has been polished beforehand. Data analyses were performed using
155 EVA software with background and $K\alpha_2$ corrections, as well as scale normalization for
156 comparison between the samples. Identification of crystalline phases was made by
157 comparison with PDF standards (Powder Diffraction Files) from ICDD (International Centre
158 for Diffraction Data).

159

160 Scanning electron microscopy (SEM) observations were performed on a Vega 3 SEM
161 (Tescan, Czech Republic) equipped with a tungsten filament and coupled to energy dispersive
162 X-Ray spectroscopy (EDX). Observations were made on gold coated samples. Images
163 acquisition was performed in back scattering electron (BSE) mode, with an acceleration
164 voltage of 5 kV. EDX acquisitions were performed with an acceleration voltage of 15 kV and
165 using an Oxford Instruments INCA x-act. Data analyses were performed using Aztec One
166 software series.

167

FTIR, TG-DTA, XRD and SEM tests were performed on grinded sample's pieces without using any hydration stop process to avoid chemical or microstructural damages. All tests were then performed after the exact curing time delay.

3. Results

3.1. Mechanical Properties

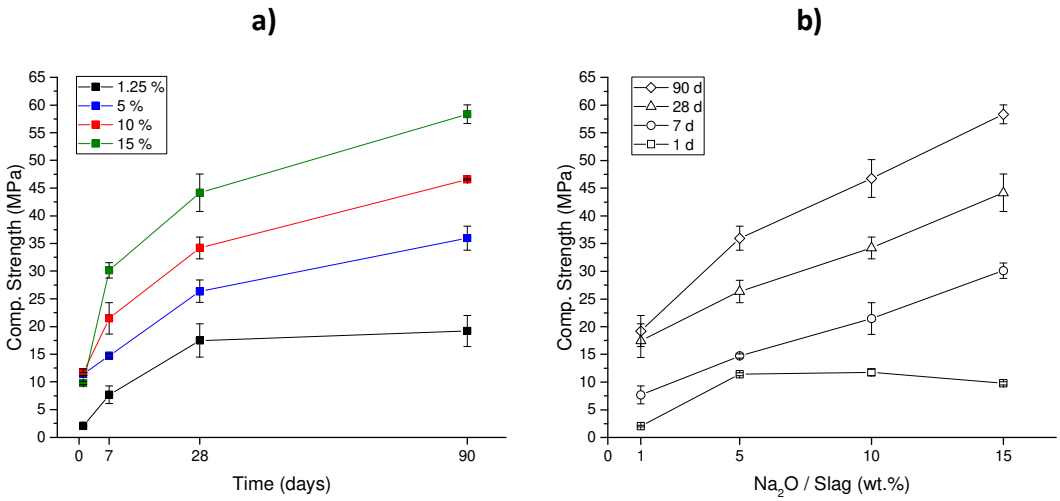

Figure 2: Evolution of compressive strength (a) for each A/S with time, and (b) for different curing time as a function of activator ratio

Evolution of compressive strength with time is displayed in Figure 2.a for different A/S ratios. After 1 day of curing, strength development is very low for 1.25% of activator and samples are almost impossible to demold properly because cohesion is not sufficiently achieved. For samples with an A/S ratio superior to 1.25%, cohesion is achieved and all samples present a compressive strength close to 10 MPa. Above this threshold, the ratio doesn't seem to noteworthy impact strength development after 24 hours [41]. This observation is made more obvious when compressive strength is plotted against sodium to slag ratio for each curing time (Figure 2.b) since for 1 day of curing strength development does not appear to be linked to activator content above 1.25%. From 7 days, compressive strength increases for each formulation, this increase being proportional to the sodium concentration. Between 1 and 7 days, compressive strength increases by a factor of 1.3, 1.8 and 3.0 for 5, 10 and 15% respectively. As it can be seen in Figure 2.b, compressive strength varies linearly with initial A/S at 7 and 28 days. This linear trend is still noted at 90 days except for 1.25% sample, since compressive strength doesn't evolve anymore after 28 days for this formulation (Figure 2.a).

Strength development above 1 day of curing strongly depends on A/S in the case of sodium hydroxide activation, especially regarding long term performances.

3.2. Early Age Hydration

Figure 3 shows FTIR spectra collected from anhydrous slag and from all hydrated samples after 24h of curing. Considering the spectrum of anhydrous slag, the broad band noted between 1550 - 1400 cm^{-1} and centered on 1475 cm^{-1} (Figure 3.b) is attributed to CO_3^{2-} vibrations in different configurations [42–46], revealing the presence of carbonated species. The broad dome visible between 1050 and 750 cm^{-1} (Figure 3.a) is mainly attributed to silico-aluminate groups which form the main structure of anhydrous slag. Finally, the presence of a band at 875 cm^{-1}, attributed to CO_3^{2-} vibrations in calcium carbonates [42,44–46], confirm the presence of $CaCO_3$ phases.

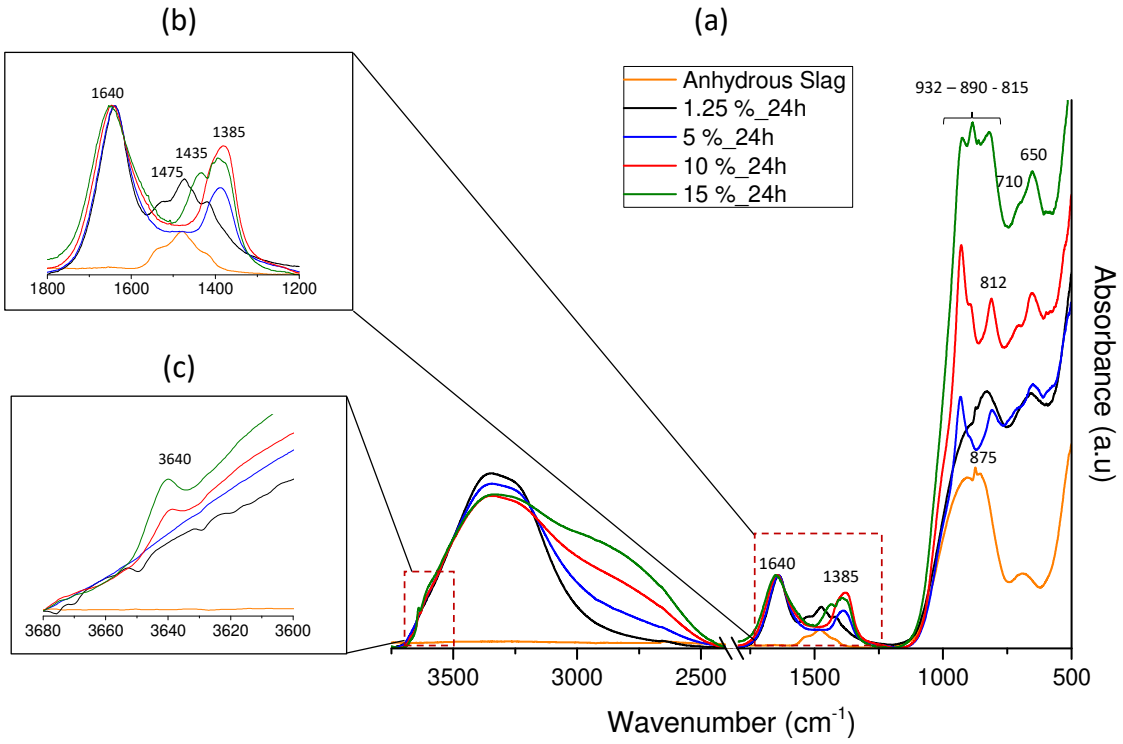

Figure 3: (a) FTIR spectra of anhydrous slag and hydrated samples for each A/S after 24 hours of curing, between 500 - 3750 cm^{-1}, (b) zoom between 1200 - 1800 cm^{-1} and (c) zoom between 3600 – 3680 cm^{-1}

Spectra of activated samples show a broad band between 3650 - 2600 cm^{-1} typical of O-H stretching vibration of hydroxyl groups from hydrated phases and from free water, the latter being also visible at 1640 cm^{-1}. The broad OH-band clearly tends to shift to lower frequencies while activator content increases. This shift is due to the dissolution of sodium hydroxide in the activating solution. It is related to Na – OH vibrations [47] and a reduction of the OH – O bound length [48] due to the structuration of water involved by the presence of soda. The specific band of portlandite ($Ca(OH)_2$) at 3640 cm^{-1}, attributed to Ca – OH vibrations [46], is clearly visible for samples with activator content above 10% (Figure 3.c) and its absorbance increases with sodium content. This result is consistent with those reported in the literature with an A/S of 8% [49]. Considering carbonates vibrations region (Figure 3.b), the specific bands of anhydrous state centered on 1475 cm^{-1} are visible for 1.25% of activator, so that anhydrous carbonated species have not been dissolved. However, for an activator content superior to 1.25%, bands at 1385 and 710 cm^{-1} differ from those of anhydrous slag, revealing a change in carbonates configuration [50]. These bands are close to those observed for dissolved carbonate anions CO_3^{2-} [43]. This is attributed to an attack of calcium carbonate phases which can leads to its partial or total dissolution. For the 15% sample, a band at 1435 cm^{-1} is attributed to the presence of hydrated sodium carbonates, $Na_2CO_3 \cdot x(H_2O)$ [32,42]. The formation of calcium silicate hydrates potentially containing high amount of aluminum, C-A-S-H [51], is revealed in the low-frequency region (500 – 1200 cm^{-1}) by the bands at 932, 812 and 650 cm^{-1} [46,51–58] (Figure 3.a). The relatively low main wavenumber associated to asymmetric stretching vibration of Si-O-T (T= Si or Al) bonds at 932 cm^{-1} could be associated to relatively depolymerized C-A-S-H, mainly composed of Q^1 or Q^2 tetrahedral units, either due to high calcium to silicon (C/S) ratio [46], sodium uptake [59] or to high amount of aluminum incorporation [46,51,52,60]. It can be noted that the bands associated to C-A-S-H gel do not shift with increasing activator content. The band at 890 cm^{-1} is not visible for 5% sample, slightly present for 10%, and well defined for 15%, indicating significant differences in the hydrated phases formed. This band is attributed to the formation of a hydrotalcite-like phase noted at early age only when A/Sis above 10%.

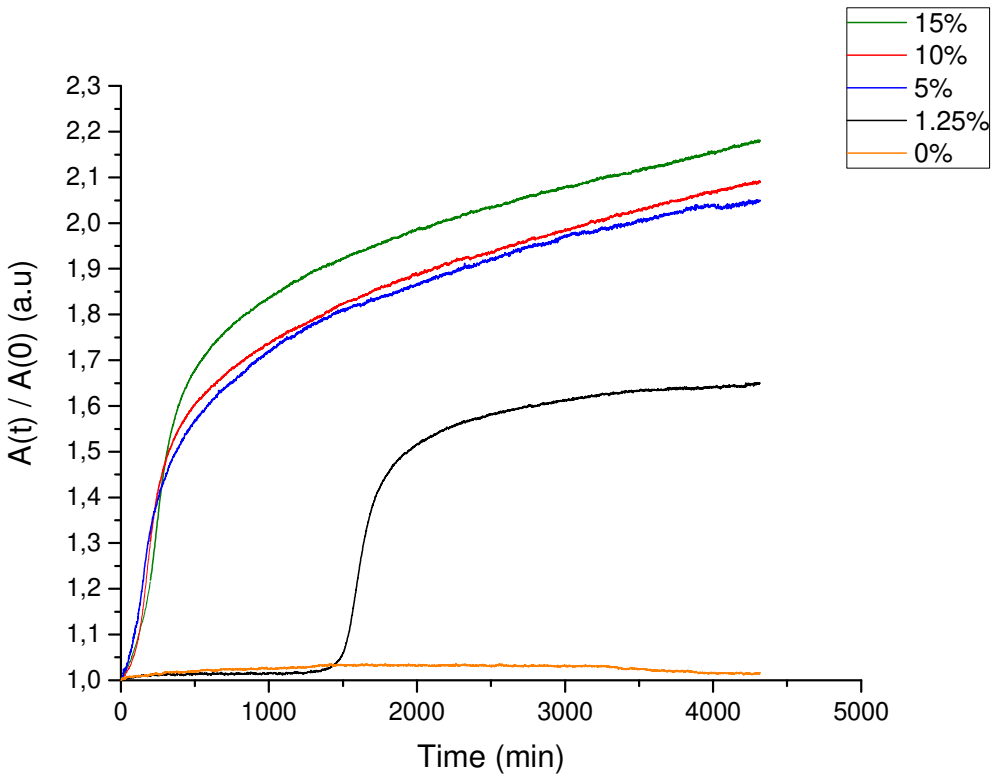

Figure 4: Evolution of normalized absorbance at 932 cm^{-1} during the first three days of curing for each A/S, obtained by FTIR in situ measurements. A(0) is the absorbance value at time t = 0 min

The continuous *in situ* acquisition of infrared spectra during the first 3 days of hydration allowed to measure the evolution with time of the absorbance of the 932 cm^{-1} band, related to C-A-S-H (Figure 4). The absorbance is normalized by its value at the beginning of the experiment. When slag is mix with free water (Na_2O = 0%), no evolution of the absorbance of the band at 932 cm^{-1} is observed. No C-A-S-H hydrates are detected during the first 3 days, which is consistent with the fact that slag hydration in water is very slow [3]. For an A/S ratio of 1.25%, first hydrates precipitation is detected around 1500 min (25 h). This result is consistent with individual measurements (Figure 3.a) and with the poor cohesion noted at 1 day (Figure 2.a). The absorbance increases then rapidly until 2500 min (42 h) before slowing down until being almost constant at a relatively low level regarding to others formulations. One can note that during the first 24 hours, *in situ* spectra of 1.25% sample and of free water present a similar shape, with no possible identification of any characteristic band of anhydrous or hydrated slag (available in the supplementary material). Since the depth of penetration of the evanescent infrared wave used in ATR mode is estimated to approx. 5 µm for those materials, it may only penetrates a thin water layer formed between slag grains and